Physica Medica 136 (2025) 105061

Contents lists available at ScienceDirect

Physica Medica

journal homepage: www.elsevier.com/locate/ejmp

Original paper

Assessment of physical phantoms produced in the PHENOMENO project utilizing three fused filament fabrication approaches☆

Kristina Bliznakova [a,b,*], Nikolay Dukov [a,b], Zhivko Bliznakov [a,b], Viktoria Petkova [b], Vencislav Nastev [b], Vasilis Eleftheriadis [c], Panagiotis Papadimitroulas [c,d], Nikiforos Okkalidis [e], Elena Ivanova [f,g], Tsvetelina Teneva [h], Georgi Todorov [f,i], Giovanni Mettivier [j,k], Paolo Russo [j,k]

[a] Department of Medical Equipment, Electronic and Information Technologies in Healthcare, Medical University – Varna "Prof. Dr. Paraskev Stoyanov", Varna, Bulgaria
[b] ELPIDA Research Group, Research Institute, Medical University – Varna "Prof. Dr. Paraskev Stoyanov", Varna, Bulgaria
[c] BIOEMTECH, Athens, Greece
[d] Medical Informatics Laboratory, School of Medicine, University of Thessaly, Larissa, Greece
[e] Morphé, Thessaloniki, Greece
[f] Diagnostic Imaging Clinic, "Saint Marina" University Hospital, Varna, Bulgaria
[g] Medical College, Medical University – Varna "Prof. Dr. Paraskev Stoyanov", Varna, Bulgaria
[h] Department of Clinical Medical Sciences, Medical University – Varna "Prof. Dr. Paraskev Stoyanov", Varna, Bulgaria
[i] Department of Imaging Diagnostics, Interventional Radiology, Medical University – Varna "Prof. Dr. Paraskev Stoyanov", Varna, Bulgaria
[j] Dipartimento di Fisica "Ettore Pancini", Università di Napoli Federico II, Napoli, Italy
[k] INFN Sezione di Napoli, Napoli, Italy

ARTICLE INFO

Keywords:
Anthropomorphic breast phantoms
3D printing
Fused filament fabrication
Materials
Breast X-ray imaging

ABSTRACT

Introduction: The aim of this study was to evaluate the suitability of three approaches in producing physical breast phantoms using the low-cost 3D printing fused filament fabrication (FFF) technique.
Methods: Three physical phantoms were produced: the first (PB1) is based on PLA filament extruded with different extrusion rates and constant printing speed; the second (PB2) and third (PB3) were each printed with two filaments: ABS-ASA for PB2 and HIPS-ASA for PB3. The phantoms were scanned using a clinical CT facility at different kilovoltage (kV) settings. Objective analysis comprised power spectrum, fractal dimensions, histogram metrics (skewness, kurtosis), and Hounsfield Unit (HU) values. Experienced radiologists performed a subjective assessment.
Results: All phantoms demonstrated β indexes in the range of 1.39–2.72, with PB2 showing the lowest values. The measured HU values for the breast tissues as a whole increased with increasing kV. PB1 showed very good results in terms of measured HU values for glandular tissue, skin, and adipose tissue. In PB2, ABS proved to be well suited for representing adipose tissue, whereas HIPS exhibited lower than expected HU values. Similarly, in PB3, ASA showed HU values that were lower than those reported in the literature. These discrepancies highlight the need for further optimization of printing parameters for HIPS and ASA materials. Subjective evaluation revealed no significant differences in the visual quality of the phantoms.
Conclusions: FFF printing challenges hinder widespread anthropomorphic phantom production. Further research is needed for dual-material printing.

1. Introduction

3D printing technology has been increasingly integrated into both research and clinical practice within the field of Radiology [1]. Many 3D printers are now used in the medical imaging field to test and optimize novel imaging modalities and algorithms as well as to perform clinical and imaging trials and training. Among the available 3D printing technologies, fused filament fabrication (FFF) is one of the lowest-cost

☆ This article is part of a special issue entitled: 'Women in Medical Physics' published in Physica Medica.

* Corresponding author at: Medical University – Varna "Prof. Dr. Paraskev Stoyanov", Varna, Bulgaria.
E-mail address: kristina.bliznakova@mu-varna.bg (K. Bliznakova).

https://doi.org/10.1016/j.ejmp.2025.105061
Received 13 May 2025; Received in revised form 18 July 2025; Accepted 21 July 2025
Available online 25 July 2025

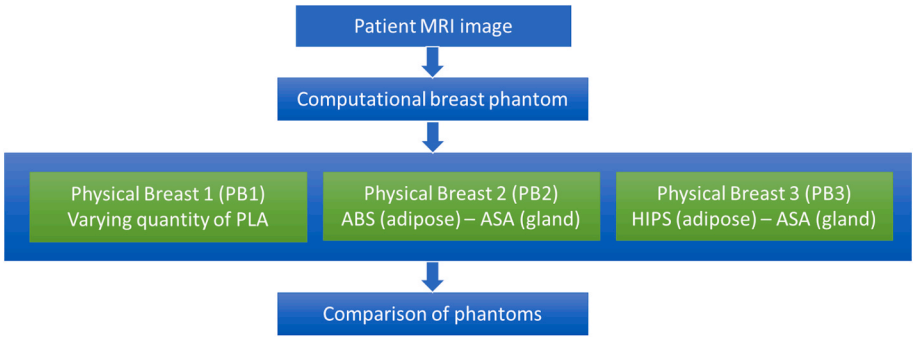

Fig. 1. Outline of the comparative study. The physical phantoms are based on a segmented MRI patient data.

options and has been used by researchers to produce phantoms for radiological medical applications [1–4]. Within this specific 3D printing technology, three main approaches lead in the creation of radiological physical phantoms. The first method involves employing different percentages of infill densities and patterns to reproduce internal structures with computed tomography (CT) Hounsfield Units (HU) close to those of body tissues. Okkalidis *et al.* [5] used this approach to print radiological anthropomorphic phantoms of the chest and skull, while Hamedani *et al.* [6] used it to create a pelvis phantom. One of the limitations of this method is the visibility of the printed pattern, which affects both the spatial resolution of FFF 3D-printed phantoms and its reproducibility. In the second approach, one adjusts the layer ratio between two different materials: Okkalidis *et al.* [7] used PLA (Polylactic Acid) and Stonefil filaments to print a hip bone of a pelvis, while Tino *et al.* [8] used standard PLA and iron powder to print bone phantoms. In this approach, challenges include *i)* the selection of suitable printing materials and addressing inherent defects associated with dual-extrusion 3D printing, particularly when extruding metal-reinforced composites; and *ii)* the limited layer thickness achievable for each filament, which may exceed the CT slice thickness, leading to visible layering patterns. The third approach involves depositing melted amounts of filaments per voxel as proposed by a few investigators to produce anthropomorphic phantoms of the breast and lung tissues [9–11]. This is achieved either by adjusting the filament extrusion rate per voxel while keeping the printing speed constant, or by keeping the extrusion rate constant across all voxels and then modifying the printing speed appropriately. For this purpose, the investigators conducted proof-of-concept studies, during which a single patient-based phantom was printed and evaluated.

All these studies involve an extensive research and calibration process to accurately correlate the HU of specific tissues with precise 3D printing settings. An alternative to FFF printing of anthropomorphic phantoms with a single material is to use several suitable materials with 100 % infill density. Such an approach is proposed by the UNINA group (Università di Napoli Federico II) [12,13], who printed anthropomorphic uncompressed breast phantoms using polyvinyl alcohol (PVA, for skin tissue mimicking), Nylon (for glandular tissue) and Acrylonitrile Butadiene Styrene (ABS, for adipose tissue). These materials simulate closely the attenuation properties of breast tissue at lower X-ray energies [14]; however, at higher X-ray energies these materials change the X-ray properties and exhibit HU values different from those of real tissues [15,16]. A 100 % nominal fill density proved sufficient to reproduce breast anatomy accurately, eliminating the typical mesh-like background associated with FFF filament-based technology [13].

An international research team, under the PHENOMENO EU-funded project, is developing methods for producing both computational and physical breast phantoms for X-ray imaging research (https://phenomeno.eu/). Recent developments within the framework of this European collaboration have resulted in a method for generating computational phantoms from breast magnetic resonance imaging (MRI) datasets, as well as physical phantoms printed with one filament at varying densities, depending on the HU of the voxel, i.e. the third approach described above [10]. Building on an extensive experimental study aiming to evaluate the suitability of both existing and novel filaments for replicating the HU of human tissues [17], we developed two novel anthropomorphic breast phantoms with 100 % infill density using this alternative printing approach. This study evaluates the three FFF-based methods for producing anthropomorphic phantoms for X-ray imaging and discusses challenges in their production.

2. Materials and methods

Fig. 1 illustrates the key methodological steps undertaken in the study. Initially, an anthropomorphic computational phantom was created based on a patient MRI dataset. The starting point was a T1-weighted image set from a contrast-enhanced patient MRI scan, which was segmented into skin, adipose, glandular and lesion tissues. The resulting 3D anthropomorphic breast phantom served as the source for the production of three physical breast phantoms: (a) physical breast 1 (PB1), produced with the method of extruding amounts of filaments as a function of the voxels' HU under a constant printing speed, (b) physical breast 2 (PB2) produced with 100 % infill density, where adipose tissue is represented by ABS, and glandular tissue is represented by ASA (acrylonitrile styrene acrylate), and (c) physical breast 3 (PB3) fabricated with 100 % infill density, where adipose tissue is represented by HIPS (high-impact polystyrene) and glandular tissue is represented by ASA.

The selection of materials representing the adipose and glandular tissue (the two main internal components of the modelled breast) is based on the study of Okkalidis *et al.* [17], where the X-ray properties of 29 materials for 3D printing were studied in both printed and melted form. As a final step, a CT image of the printed phantoms was acquired with a clinical CT unit; selected slices were evaluated in terms of specific features, profiles through slices and measured HUs.

2.1. Computational phantom

The computational phantom was developed using a T1-weighted image set from a contrast-enhanced MRI scan of the right breast of a 57-year-old patient diagnosed with invasive ductal carcinoma [10]. The acquisition of the patient's MR image sets was performed with a GE Signa HDxt MRI scanner, with a voxel size of $0.7 \times 0.7 \times 0.8$ mm^3. The MR image was segmented into skin tissue, glandular tissue, adipose and lesions. Initially, a threshold operation was performed to separate the tissue of interest, followed by a series of few morphological operations, which reduce the number of artifacts. Adipose tissue was derived indirectly through the segmentation process of three primary tissues: skin, glandular, and lesion. These three segmented tissues were merged into a single composite object. Next, we created a mask resembling the size and shape of the segmented skin, but with infill to encompass the entire breast. This mask was then used to identify the adipose tissue by calculating the difference between the composite object, formed by the three tissues and the generated mask. Finally, we combined all tissue

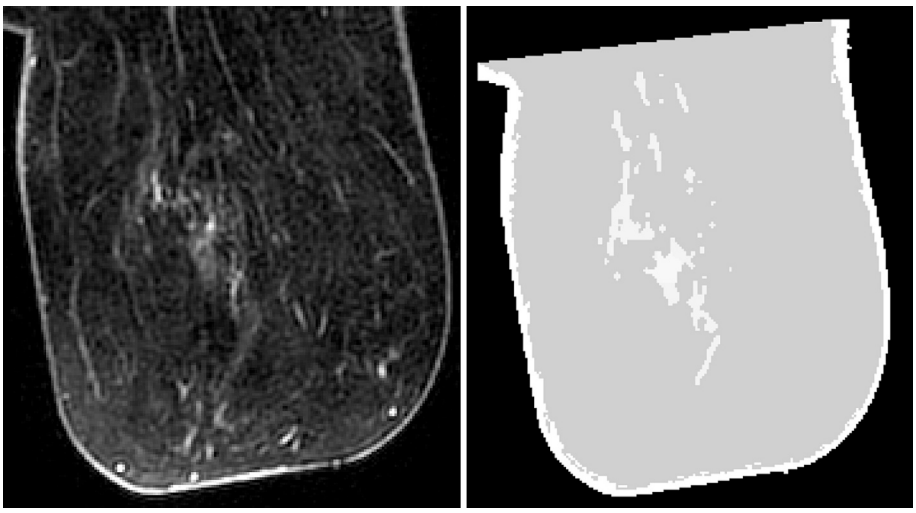

Fig. 2. An image from the original dataset of patient images (left) and a segmented breast slice (right) used in the 3D printing procedure.

Table 1
Materials used to fabricate the physical phantoms (3D-printed) in the study.

Manufacturer	Polymer type	Printing temperature, ℃	Temperature of working plate, ℃	Density, g·cm^{-3}	3D printer
FormFutura	HIPS	230	90	1.05	Raise3D Pro3 Plus
FormFutura	ASA	260	90	1.11	Bambu Lab X1-Carbon Raise3D Pro3 Plus
LeapFrog	ABS	270	90	1.02	Bambu Lab X1-Carbon
Formfutura	PLA	180	60	1.24	Multoo MT2-B

components – skin, glandular, lesion, and adipose – to construct the complete computational model of the breast, Fig. 2.

The segmented tissues were also assigned HU values as follows: –152 HU for adipose tissue, 42 HU for glandular tissue, 108 HU for skin, 64 HU for lesion. These values correspond to the average HU values of these tissues for 80 kV CT imaging.

2.2. Physical phantoms

2.2.1. PB1 phantom

We created this phantom by using the 3D printing method based on adjusting the filament extrusion rate to match the HU values derived from each voxel in the prepared patient's CT DICOM image set. To replicate glandular and lesion tissues, which are characterized by more irregular shapes, a perimetric printing pattern was employed [10]. To print the phantom we adopted the Multoo MT2-B 3D printer, equipped with a Volcano Hotend extruder and a 0.4 mm nozzle. The selected filament was EasyFil PLA (Formfutura, Netherlands, $\rho = 1.24$ g/cm^3, a diameter of 1.75 mm), and the extruder temperature was set to 180 °C. The printing speed was kept constant at 30 mm/s, the heated bed was maintained at 60 °C and the layer height was set to 0.25 mm, considering the slice thickness of the MR image data. This 3D printing technology was developed by Morphe [18], and the printer was calibrated to reproduce the segmented structures accurately. Printing time was seven days.

2.2.2. PB2 and PB3 phantoms

Our recent study on materials used for production of radiology phantoms included the investigation of the CT numbers of 29 commercial and custom filaments, suitable for 3D printing, utilizing fused filament fabrication technology [17]. We determined the average and standard deviation of HU values of these materials by scanning test samples with the clinical CT unit, with tube voltages from 80 kV to 120 kV. The CT numbers for each material were analyzed, and sets of filaments were identified as potential representatives of breast tissues: Thermoplastic copolyester [19] and ASA for glandular tissue and HIPS, and ABS for the adipose tissue. Table 1 summarizes the materials used as filaments for printing the physical radiological models and their

Fig. 3. Printed breast phantoms: (left) Physical breast phantom PB2 from ABS-ASA, (middle) Physical breast phantom PB3 from HIPS-ASA and (right) Physical breast phantom PB1 from PLA.

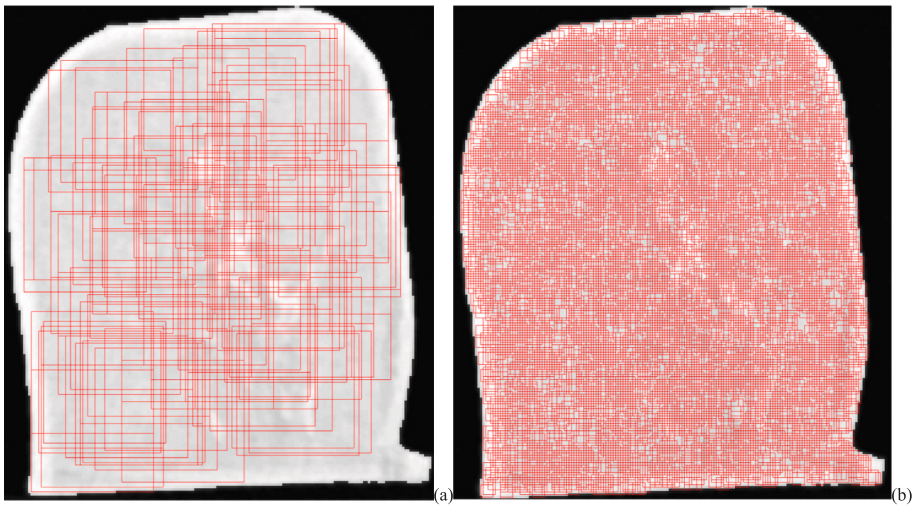

Fig. 4. Objective evaluation of the physical phantoms: (a) Regions of Interest (ROIs) of 50 × 50 pixels were used to evaluate the β exponent and the fractal index, while (b) ROIs with 5 × 5 pixels and 2 × 2 pixels were used for evaluation of HU values, skewness and kurtosis.

working temperatures.

Physical breast PB2 was produced using ASA and ABS materials with X1-Carbon Bambu Lab printer (Bambu Lab, https://bambulab.com/). These filaments offered a distinct advantage for the experiment due to their similar printing temperatures and chemical composition. Bambu Studio Slicer was used to prepare the STL file of the computer model for printing. Printing time was approximately three days.

Physical breast PB3 was fabricated using HIPS material for adipose tissue, and ASA for glandular tissue substitutes. This phantom was printed with Raise3D Pro3 Plus (https://www.raise3d.com/products/raise3d-pro3-plus-3d-printer). The ideaMaker Slicer was used to prepare and "slice" the 3D model. To prevent oozing from inactive extruders, the ASA extruder was maintained at 220 °C (40 °C below its printing temperature), and the HIPS extruder was kept at 180 °C (50 °C below its printing temperature) during the printing process. Printing time was five days.

2.3. Experimental setup and processing

The three phantoms were scanned at a clinical CT facility. The CT protocol used was Thorax, with a reconstructed slice thickness of 1 mm and tube voltages 70 kV, 80 kV, 90 kV and 120 kV. Phantoms slices were reconstructed with 512 × 512 pixels, with each pixel measuring 0.275 × 0.275 mm^2, resulting in a total slice size of 141 × 141 mm^2. Fig. 3 shows the test objects positioned on the CT couch before acquiring the CT data.

We adopted subjective and objective approaches to carry out a preliminary evaluation of the proposed methodology for 3D-printed physical breast models. The objective evaluation compared the HU values among the different phantoms, and with those reported in the literature for clinical 3D breast images. It also involved calculating skewness, kurtosis, and conducting fractal and power spectral analyses. The evaluation was carried out by using the Matlab tool developed by Marinov *et al.* [20] for three non-consecutive slices from each physical phantom.

Skewness, kurtosis, HU mean and HUs histograms were assessed for the whole breast through Regions of Interests (ROIs) defined with size of a 5 × 5 pixels in order to reflect local changes in the breast texture (Fig. 4b). HU values for skin, adipose and glandular tissues were assessed by using a 2 × 2 pixels ROI defined throughout the entire breast region. In this way, the glandular tissue of the segmented phantoms was represented by very small and narrow areas. This approach was necessary because when a larger ROI was positioned, the average values of the ROI were affected by the background. A total of 6000 ROIs were analysed for each kilovoltage (kV) setting and for each phantom.

Table 2
Questions used for the evaluation of the physical breast phantoms.

Question	Answers
1. Does the image contain any visible lesions?	**A.** Yes **B.** No **C.** Uncertain
2. Does the lesion appear realistic?	**A.** Yes, completely realistic **B.** Partially realistic **C.** Not realistic
3. What is the type of the lesion observed?	**A.** Benign **B.** Malignant **C.** Calcification **D.** Cystic **E.** Other
4. Can you clearly differentiate between the various breast components?	**A.** Yes, they are clearly distinguishable **B.** Some differences are observed, but not always perfectly clearly. **C.** No, the breast components all look the same.
5. Are the modelled breast components realistic in appearance?	**A.** Yes, highly realistic **B.** Somewhat realistic **C.** Not realistic at all
6. Does the breast model, as a whole, appear realistic?	**A.** Yes, very realistic **B.** Moderately realistic **C.** Not realistic

Scoring Points: Correct detection = 1; Incorrect detection = 0; Uncertain = 0.5.
Yes, completely realistic = 1; Partially realistic = 0.5; Not realistic = 0.
Correct identification = 1; Incorrect identification = 0; Partial match = 0.5.
Yes, they are clearly distinguishable = 1; Some differences are observed, but not always perfectly clearly = 0.5; No, the breast components all look the same = 0.
Yes, highly realistic = 1; Somewhat realistic = 0.5; Not realistic at all = 0.
Yes, highly realistic = 1; Moderately realistic = 0.5; Not realistic at all = 0.

The spectral analysis involved calculating the β parameter from the slope of log–log 1D noise power spectra, considered as a quantitative measure of anatomical complexity or noise in healthy breast tissue texture [13,21,22]. This parameter was evaluated to assess how well the developed phantoms replicate the anatomical noise patterns found in real clinical images. Typically, β values are around 3 in digital mammography and breast tomosynthesis images, and decrease to approximately 2 in CT images where anatomical noise is less prominent [21–25]. To estimate the β parameter, we calculated 3000 randomly selected ROIs of 50 × 50 pixels, in each of the three evaluated CT slices, as shown in Fig. 4a. The fractal index was also deducted from these ROIs.

Finally, a task-based evaluation was designed for the physical breast phantoms. The study involved two experienced radiologists, trained within the PHENOMENO project. The design of this study was influenced by our previous work [10], with the questions and points assigned to each answer, summarized in Table 2. They were formulated to represent various scenarios for assessment, where the different structures in a breast phantom were observable or not. The assigned points

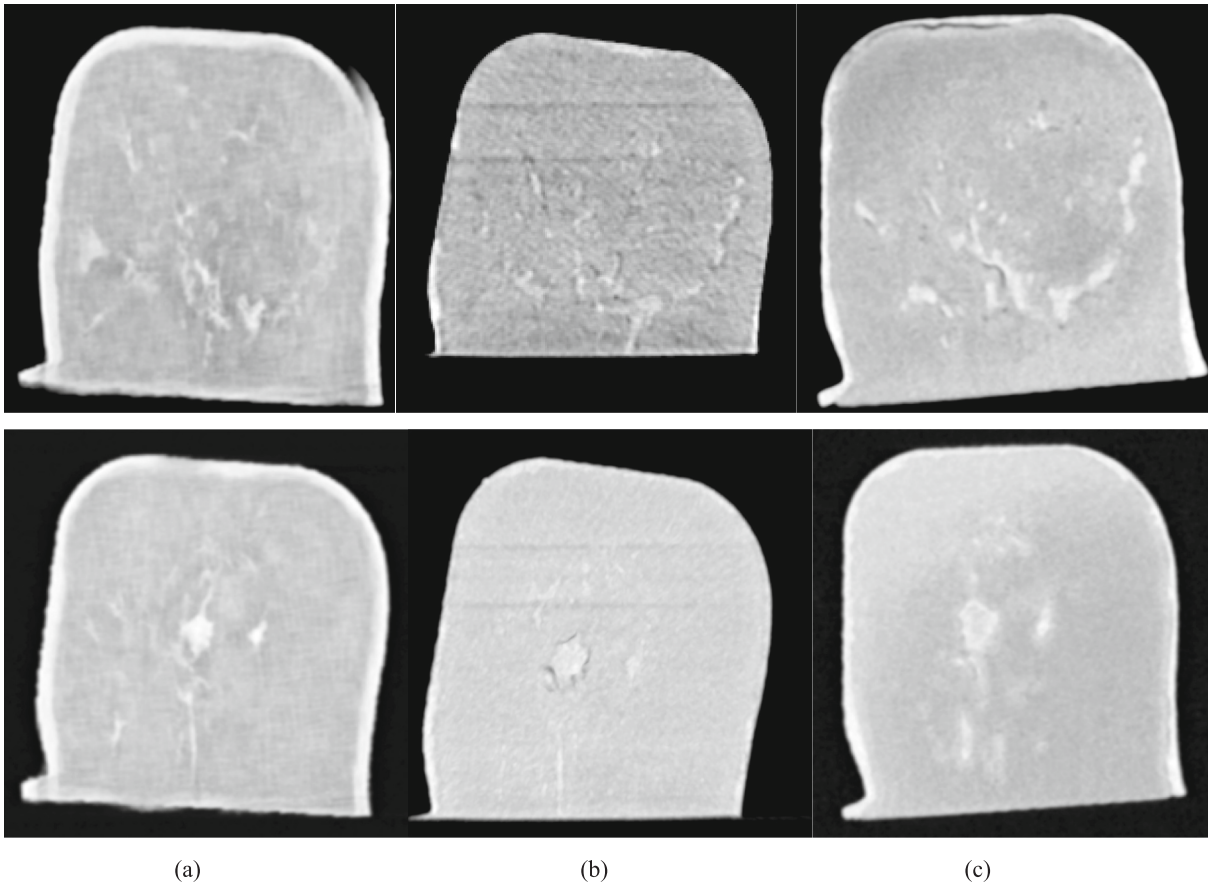

Fig. 5. Selected CT slices used in the evaluation of phantoms: (a) PB1, (b) PB2, and (c) PB3.

were then summed for each phantom technology. The maximum possible score was 30 for PB1 and 36 for PB2 and PB3, respectively. Finally, the performance of each technology was calculated as a percentage ratio of the collected points vs. the maximum possible points.

3. Results and discussion

3.1. Comparison of Hounsfield Units of selected tissues

Fig. 5 shows CT slices from the scanned breasts used in both subjective and objective evaluation. Visually, all phantoms provided apparent contrast between glandular and adipose tissues, as the highest visible contrast is observed in the PB1 and PB3 phantoms. The main reason for the lines seen in the CT image of PB2 phantom (Fig. 5b) was the partial clogging of the nozzle, preventing the deposition of material for that layer or a portion of it. Upon discovery of the clogging issue, the printing was paused and then resumed after clearing the nozzle. Further on, air gaps between the lesion and the neighbouring structures in PB2 are also visible, as shown in the lower row of Fig. 5b. The most likely contributing factors to this issue are the default printing settings used and the smoothing process during the segmentation of the different tissues. Furthermore, the Bambu Studio slicer demonstrated limitations during the slicing process, because of the inability of the slicing algorithm to cover the whole surface area of a layer with an uneven shape using 0.4 mm lines. This phantom was printed as a single object unlike the other two phantoms, which were printed in thick slices.

Printing the PB1 phantom required a custom-designed 3D printer controlled by specialised software based on DICOM images. This unique setup led to a slow printing process. To ensure successful fabrication, we decided to print PB1 in multiple parts rather than as a single unit, which also necessitated continuous monitoring. Printing the PB3 phantom required a dual-nozzle 3D printer for the two distinct filaments. We specifically used the Raise3D printer for this purpose due to its dual-nozzle functionality. However, throughout the printing process, the nozzle dispensing the HIPS filament consistently clogged. As a result, the PB3 phantom was printed in multiple separate parts, as well. We have been investigating solutions for this persistent issue for more than a year.

Fig. 6 summarises the comparison of HU values (mean ± std. dev.) for the printed tissues across the three methods. For PB1 phantom, the simulated tissues showed similar values as the kV setting increased. For adipose and skin printed tissues, the HU value slightly increases with increasing kV, consistent with the observed trend for PLA in experimental studies [15,26]. This trend also correlates with the adipose tissue data within this kV interval [16]. For glandular tissue, the measured HUs show a relatively consistent trend. However, the large standard deviation prevents a confident conclusion that HU values significantly change with anode voltage. This suggests further experimentation with a breast of higher density. For PB2, ABS was used to represent the breast adipose tissue. As seen from Fig. 6, it increases with increasing kV. This is well supported by experimental data from ABS samples, scanned at different kV settings [15,17] and has been shown by several investigators to be an appropriate material for representing the adipose tissue [12,17,27].

HIPS material is a polymer that recently gained more attention for usage in 3D printing of phantoms. Results from experimental studies showed that this material may be appropriate for representing breast adipose tissue [17,27]. However, during the phantom manufacturing of PB3, we encountered numerous failures, primarily attributed to the material itself. HIPS is manufactured by various companies, and based on our printing experience it shows significant quality variations between different brands. Additionally, tuning critical printing parameters, such as temperature and speed, proved essential. Printing different

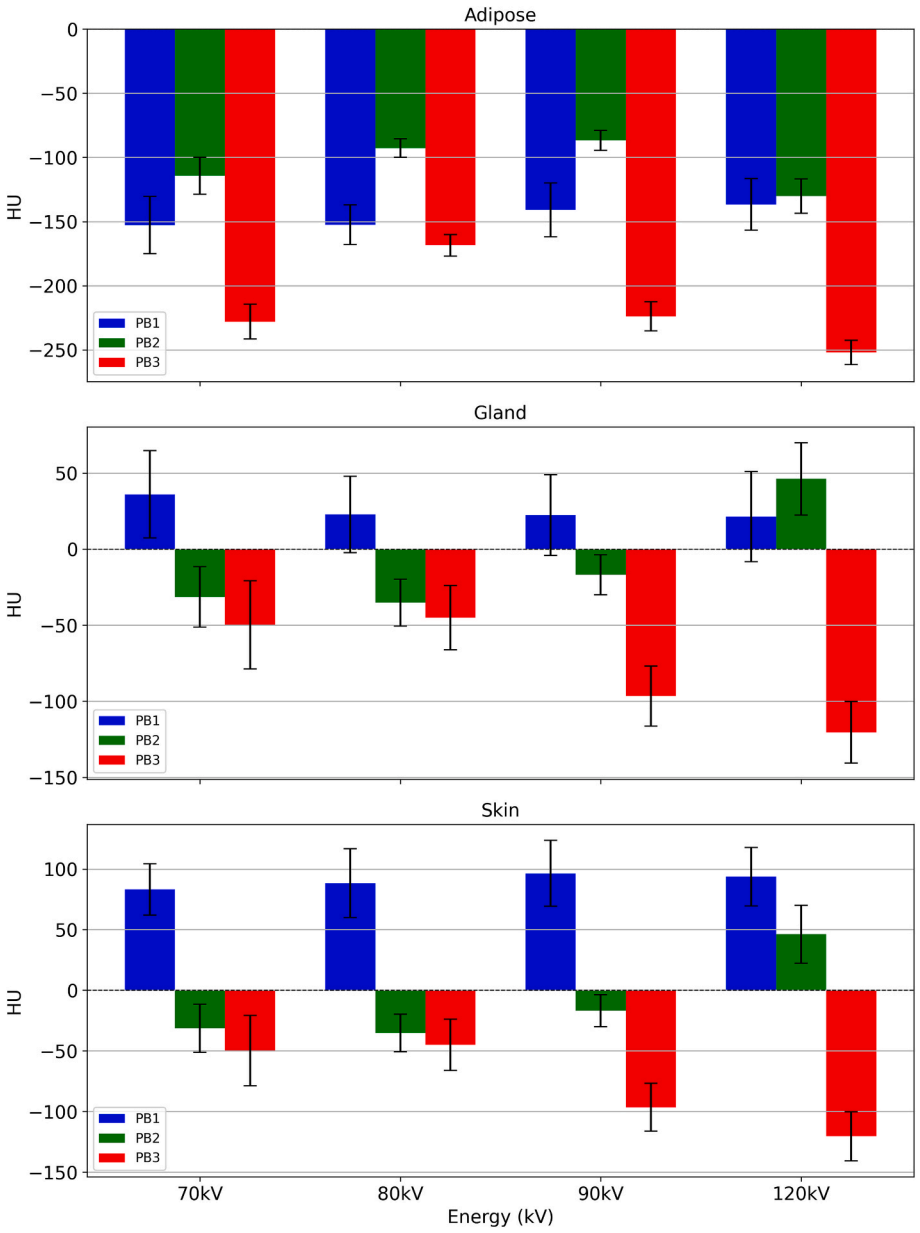

Fig. 6. Averaged HU values for glandular, adipose and skin printed tissues in PB1, PB2 and PB3.

parts of the breast model using various slicers and materials from different manufacturers introduced further complications and significantly extended the process. Despite these challenges, the low HU values observed in our evaluation for adipose tissue align well with the HU values of ABS and PLA in the other two phantoms and with the results reported by Okkalidis *et al.* [17], for HIPS-printed samples. Therefore, further experimental efforts in this direction will continue, aiming to develop a suitable anthropomorphic phantom with adipose tissue represented by HIPS.

In our previous study we investigated the HU of various materials, based on two approaches: by using 3D-printed 100 % infill cubes and cast samples, prepared from each studied material [17]. For the cast samples, the material filament was chopped into solid pellets and placed into a specially prepared cast and then heated near their melting point. This permitted the comparison of void-free samples to 3D-printed ones and determine the impact of air voids on HU measurements. Related to this, a key conclusion from the PB3 results is that, when comparing HU values from anthropomorphic phantoms to those of printed and melted samples from our recent study, it becomes evident that material selection should be based on the HU values of the 3D-printed samples, rather than the melted ones. This conclusion is further supported by the behaviour of ASA material in the PB2 and PB3 phantoms, when used to represent glandular and skin tissues. The measured HU values of the ROIs with ASA differ from our recent evaluation of ASA-printed samples showing HU values ranging from −9 HU at 80 kV to +3 HU at 120 kV, and HU values of +43 HU and +65 HU, respectively for printed and melted ASA samples. This discrepancy leads to poor reproduction of glandular tissue in the PB2 and PB3 phantoms. Another limitation arises from the use of a ROI measuring 2 × 2 pixels for the gland and skin measurements. Due to the small glandular and skin quantity as well as the low contrast of glandular structures on the CT images, such ROIs may not be representative. A more robust comparison can be achieved by analysing the full HU histogram for the entire CT images, as shown in Section 3.3. An alternative approach involves the manual and precise selection of pixels from approximately 20 distinct regions, resulting in a broader dataset of measurements. These values, which correspond to glandular and skin tissues at various energy levels are summarized in Table A1 of the Appendix. They demonstrate an improved correlation

Table 3
Measured values for selected features, extracted from the physical phantoms.

	Parameter	70 kV	80 kV	90 kV	120 kV
PB1	β	2.26 ± 0.34	2.53 ± 0.30	2.31 ± 0.31	2.72 ± 0.53
PB2		1.39 ± 0.28	2.01 ± 0.23	1.20 ± 0.25	1.78 ± 0.27
PB3		2.08 ± 0.27	2.28 ± 0.44	2.20 ± 0.40	2.25 ± 0.23
PB1	Skewness	0.01 ± 0.62	0.07 ± 0.60	0.00 ± 0.60	0.01 ± 0.61
PB2		0.09 ± 0.72	−0.09 ± 0.57	−0.07 ± 0.61	−0.09 ± 0.59
PB3		0.26 ± 0.68	0.16 ± 0.68	0.16 ± 0.62	0.22 ± 0.63
PB1	Kurtosis	2.55 ± 0.91	2.65 ± 0.89	2.52 ± 0.88	2.50 ± 0.90
PB2		3.66 ± 6.36	2.63 ± 0.87	2.67 ± 1.07	2.60 ± 0.90
PB3		2.85 ± 1.09	2.78 ± 1.19	2.69 ± 1.11	2.70 ± 1.11
PB1	Fractal	2.73 ± 0.09	2.73 ± 0.08	2.74 ± 0.08	2.69 ± 0.08
PB2	index	3.07 ± 0.07	2.84 ± 0.06	2.99 ± 0.06	2.94 ± 0.05
PB3		2.59 ± 0.08	2.52 ± 0.06	2.60 ± 0.106	2.51 ± 0.07
PB1	HU_{mean}	−134.7 ± 37.03	−128.02 ± 31.45	−120.86 ± 35.96	−121.14 ± 36.19
PB2		−109.03 ± 21.84	−95.43 ± 7.23	−83.57 ± 16.18	−68.23 ± 15.19
PB3		−221.77 ± 31.47	−147.58 ± 15.95	−190.50 ± 22.45	−197.9 ± 21.69

with data from our prior research. Nevertheless, this should be explored more extensively. Alongside with the efforts to optimize ASA printing parameters, current work also focuses on evaluating alternative materials such as PETG (Polyethylene Terephthalate Glycol) and Nylon as potential replacements for ASA.

3.2. Comparison of selected features

Measured values for selected features are listed in Table 3, based on evaluation of the whole breast image. These were used to objectively assess the realism of the produced phantoms and therefore the method for their production.

The analysis of the β parameter in the phantom images indicates that the anatomical noise characteristics resemble those observed in clinical 3D breast images, with β values around 2. Analysis of the power spectra demonstrated a similar trend in the β exponent for the three phantoms, which is in agreement with the β value of 2.11 ± 0.55 obtained from 180 clinical breast CT images [24]. Further, Boone *et al.* [23] analysed clinical breast CT data from 43 patients showing an average $\beta = 1.86 \pm 0.38$, while in the case of the segmented phantoms this β was 2.06 ± 0.32 for 80 kV.

Fractal analysis revealed that the phantoms' fractal dimension exhibited minimal change across the tested kV settings. The comparison of fractal dimensions among PB1, PB2, and PB3 shows that higher fractal dimensions are associated with lower β values in their respective images, a trend supported by other studies [22]. As reported in the past, reduction in breast density is related to lower anatomical complexity and higher fractal dimension [28–30]. The range of measured fractal dimensions reported in this study is between 2.5 and 3.0, corresponding to a lower breast density, which accurately reflects the actual characteristics of the mimicked breast tissues.

Results for skewness at different kV settings indicate that although the printed breast phantoms are predominantly fatty, the skewness values are not clearly negative, as we would expect with predominantly low HU values around −100 HU, typical for fatty tissue. Most of the skewness values fall within the narrow range of −0.1 to +0.3, indicating an almost symmetrical distribution. This can be attributed to several factors such as the HU values being tightly clustered, and the selected ROIs being relatively homogeneous, both of which naturally lead to skewness values close to zero. Additionally, the low resolution of the CT images may blur fine tissue details, further reducing asymmetry in the HU distribution. Since the ROIs contain mixed tissue types, even a small presence of glandular tissue can elevate the HU values and contribute to a more balanced histogram. Finally, the phantom's structure, being 3D printed with materials that do not perfectly replicate the radiological properties of real adipose tissue, may also affect the distribution, particularly at certain energy levels.

Kurtosis values are in the range of 2.5–3.66, with lower values

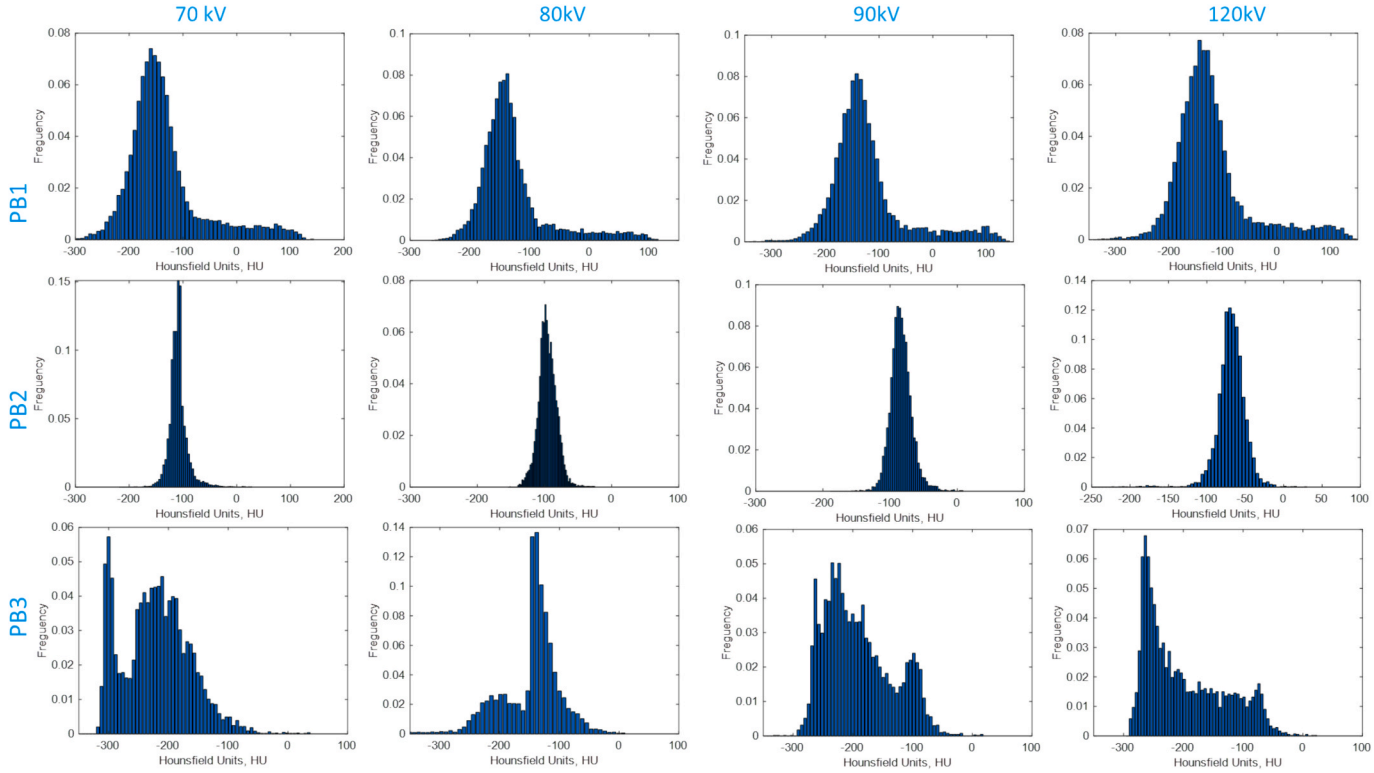

Fig. 7. Comparison of histograms of mean HU values for the three breast phantoms and different kV settings.

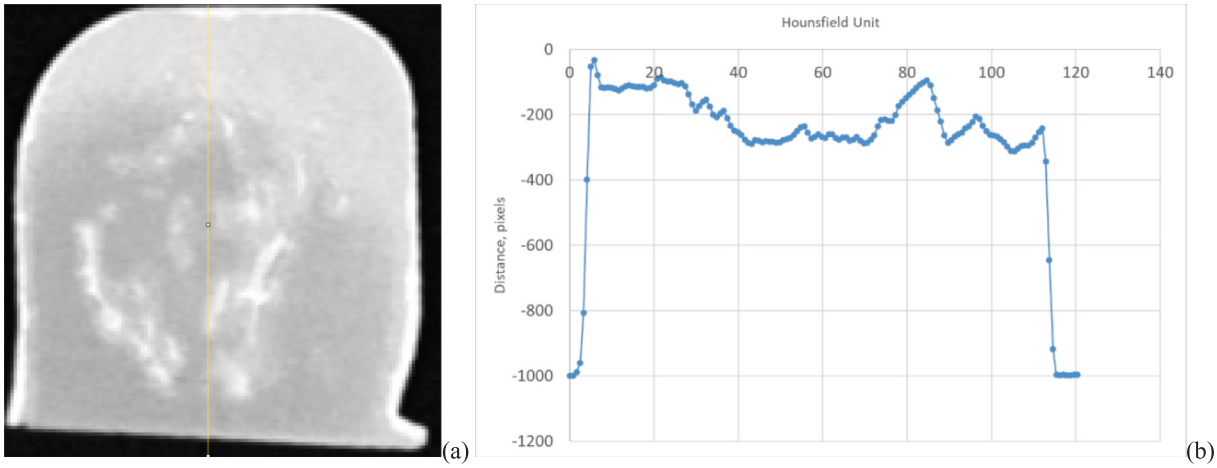

Fig. 8. HIPS-ABS phantom printing challenges: (a) Breast CT slice. (b) Vertical profile demonstrating the reduction in HU values within the printed HIPS (adipose-simulating) structure.

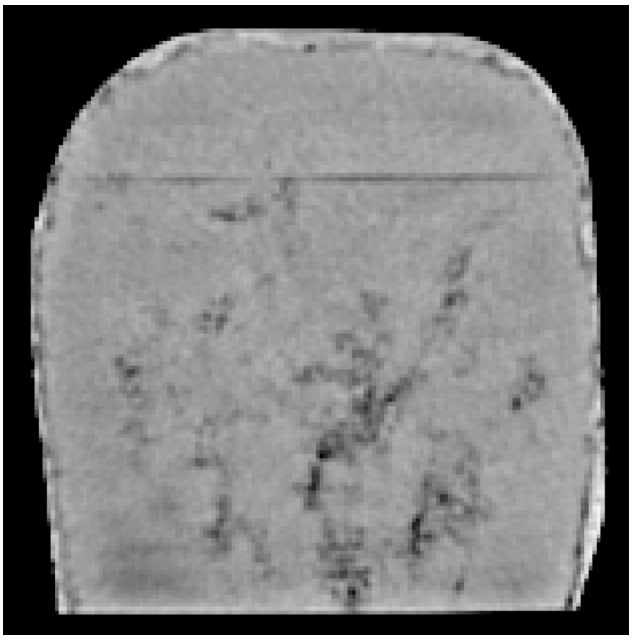

Fig. 9. A CT image from a second physical phantom produced using PB2 technology from the same computational model as the first PB2.

observed for phantom PB1. Kurtosis measures the peakedness and tail weight of a distribution. In nearly all cases, the mean kurtosis values for all physical phantoms were less than 3, which aligns with the low breast density characteristics of the phantoms used in this study.

Finally, the mean HU values for PB1 and PB2 increase with increasing kV, which is expected given that the breast phantoms are predominantly fatty and that increasing kV results in increased adipose HU values. The difference observed in the mean HU value for PB3 for 80 kV imaging may be explained by the fact that the imaging sets were obtained four months later than the rest of the images and this time gap may have influenced the exact position of this phantom on the CT table.

3.3. Histogram comparison of mean HU values

Fig. 7 depicts histogram distributions of the mean HU of the selected CT scans of the produced physical breast phantoms, shown in Fig. 5, obtained for CT scans at 70 kV, 80 kV, 90 kV and 120 kV. One can observe that the same histogram shape is preserved for both PB1 and PB2 phantoms. The peak of the histogram of PB1 is around −152 HU, which well coincides with the initially set −152 HU for adipose tissue at 80 kV for the digital phantom [10]. The histogram distributions of PB2 for the different kV settings fall within the reported adipose HUs [16,17], which is expected since the evaluated density of the digital breast phantom is 11 %, i.e. mostly fatty breast.

The histogram shape of PB3 is broader compared to PB1 and PB2. A possible reason for this is poor layer adhesion during printing which may result in trapped air, lowering HU values. This can clearly be seen from the image and the line profile in Fig. 8. HIPS absorbs some moisture, but expansion is minimal and rarely exceeds 0.1 %–0.2 % in volume, even under high humidity. In addition, the coefficient of linear thermal expansion is between 5 and 20 $\times$ 10^{-5} $^{\circ}C^{-1}$, suggesting minimal dimensional changes due to temperature variations. These two factors are excellent characteristics for fabricating 3D-printed anthropomorphic phantoms.

Finally, the ABS-ASA technology yielded promising HU results when increasing kV; however, challenges were encountered during the printing process. In one repeated printing attempt, components requiring ASA experienced extrusion failures, as illustrated in the CT image in Fig. 9. The image clearly shows that ASA was not properly extruded in the gland and lesion regions, leading to the formation of air voids. These issues were primarily attributed to the type of slicer used and suboptimal printing parameters, such as nozzle temperature, print speed, and extrusion rate. Ongoing efforts are focused on reprinting this breast phantom multiple times to optimize the settings and ensure consistent material deposition.

3.4. Subjective evaluation

An overall subjective evaluation of the three technologies is presented in Fig. 10. As seen from this summary, the first radiologist preferred the second technology, the ABS-ASA, while the second radiologist preferred the first technology, i.e. the use of single PLA. When taking both responses into account, it is evident that all three technologies scored almost the same points, with slightly higher score (by 1.39 %) for the first technology. In detail, both radiologists correctly marked the images that have the lesions. They both noted that these are malignant and that the first (PB1) and the third method (PB3) look more realistic compared to the second technology (PB2). In the second method, using ASA-ABS, the image looks only partially realistic. The reason for this is that segmented parts were initially smoothed before being combined into one matrix and there were places with empty pixels exactly on the tumour border. This observation aligns with the first radiologist's comment that the ductal structures in PB1 appeared

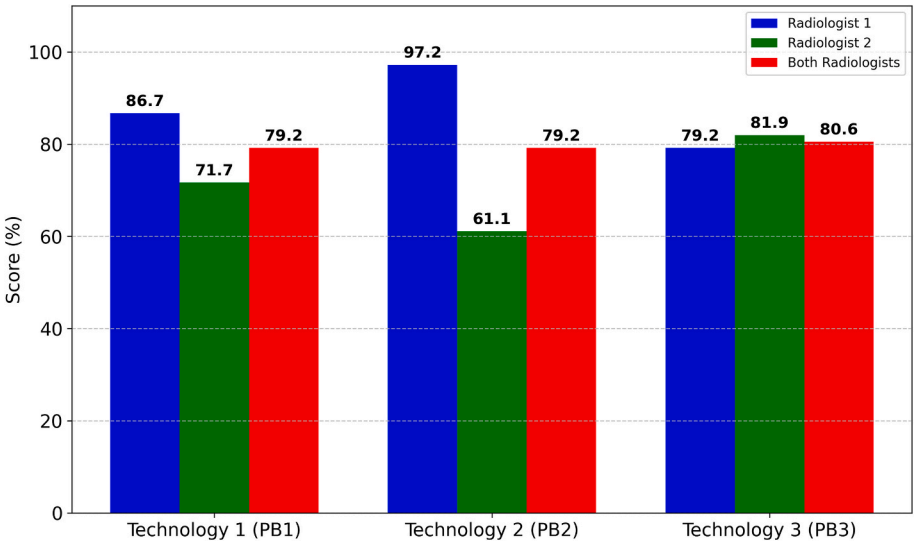

Fig. 10. Summary of results from the subjective evaluation of the three approaches for printing anthropomorphic phantoms.

unexpectedly dense (Fig. 5a), for PB2 the characteristic hypodense halo often observed around tumours was notably absent in these printed structures (Fig. 5b), while a significant issue was identified in PB3, where the skin layer presented with severe and unrealistic thickening (Fig. 5c). These observations highlight challenges in accurately replicating the density and structural features of breast tissue using these printing methodologies.

The results of this study indicate that an optimal material for 3D-printed anthropomorphic phantoms remains elusive with current FFF-based printing technology. Issues such as material shrinkage and different material characteristics persist. Therefore, extensive research is crucial to determine the most appropriate settings, particularly temperature, extrusion, and flow rates, and their compatibility with other phantom components. Furthermore, printer nozzle size significantly impacts printing accuracy and should also be considered.

4. Conclusions

The development of anthropomorphic phantoms for breast imaging using FFF shows promising potential, particularly with materials such as ABS for adipose tissue or PLA with varying densities. While some materials like HIPS and ASA currently yield suboptimal HU values for soft tissue representation, these limitations can likely be addressed through further refinement of printing parameters and material formulations. Despite variations in HU accuracy, the subjective quality of the printed phantoms remained consistently high. Overall, continued research is essential to improve material compatibility and achieve reliable, tissue-equivalent phantoms for CT imaging applications.

Use of AI tools

The authors did not use AI in this work.

Declaration of competing interest

The authors declare that they have no known competing financial interests or personal relationships that could have appeared to influence the work reported in this paper.

Acknowledgments

The PHENOMENO project “Physical breast anthropomorphic models and technology for their production” has received funding from the European Union’s Horizon 2020 research and innovation programme under the Marie Skłodowska-Curie grant agreement No 101008020

Appendix 1

Measured HU values for PB2 and PB3 based on manual and precise selection of pixels from approximately 20 distinct regions are shown in Table A1.

Table A1
Measured HU values based on manual selection in 20 regions.

	kV	HU for PB2	HU for PB3
Adipose	70	−115	−205
	80	−92	−141
	90	−94	−227
	120	−79	−223
Gland	70	−7	−20
	80	−45	−42
	90	2	−5
	120	9	3

(*continued on next page*)

Table A1 (*continued*)

	kV	HU for PB2	HU for PB3
Skin	70	26	30
	80	36	12
	90	35	32
	120	45	24

References

[1] Okkalidis N. 3D printing methods for radiological anthropomorphic phantoms. Phys Med Biol 2022;67:15TR04.
[2] Bliznakova K. The advent of anthropomorphic three-dimensional breast phantoms for X-ray imaging. Phys Med 2020;79:145–61.
[3] Hatamikia S, Gulyas I, Birkfellner W, Kronreif G, Unger A, Oberoi G, et al. Realistic 3D printed CT imaging tumor phantoms for validation of image processing algorithms. Phys Medica 2023;105.
[4] Habeeb Y, Zorn PE, Blindauer F, Kharouf N, Semeril D, Bierry G, et al. High-fidelity anatomical phantoms for MRI practical training. Phys Med 2024;127:104832.
[5] Okkalidis N. A novel 3D printing method for accurate anatomy replication in patient-specific phantoms. Med Phys 2018;45:4600–6.
[6] Hamedani BA, Melvin A, Vaheesan K, Gadani S, Pereira K, Hall AF. Three-dimensional printing CT-derived objects with controllable radiopacity. J Appl Clin Med Phys 2018;19:317–28.
[7] Okkalidis N, Bliznakova K, Kolev N. A filament 3D printing approach for CT-compatible bone tissues replication. Phys Medica 2022;102:96–102.
[8] Tino R, Yeo A, Brandt M, Leary M, Kron T. The interlace deposition method of bone equivalent material extrusion 3D printing for imaging in radiotherapy. Mater Des 2021;199:109439.
[9] Okkalidis N, Bliznakova K. A voxel-by-voxel method for mixing two filaments during a 3D printing process for soft-tissue replication in an anthropomorphic breast phantom. Phys Med Biol 2022;67.
[10] Dukov N, Bliznakova K, Okkalidis N, Teneva T, Encheva E, Bliznakov Z. Thermoplastic 3D printing technology using a single filament for producing realistic patient-derived breast models. Phys Med Biol 2022;67.
[11] Mei K, Geagan M, Roshkovan L, Litt HI, Gang GJ, Shapira N, et al. Three-dimensional printing of patient-specific lung phantoms for CT imaging: emulating lung tissue with accurate attenuation profiles and textures. Med Phys 2022;49:825–35.
[12] di Franco F, Mettivier G, Sarno A, Varallo A, Russo P. Manufacturing of physical breast phantoms with 3D printing technology for X-ray breast imaging. IEEE Nucl Sci Conf R 2019. 5.
[13] Varallo A, Sarno A, Castriconi R, Mazzilli A, Loria A, del Vecchio A, et al. Fabrication of 3D printed patient-derived anthropomorphic breast phantoms for mammography and digital breast tomosynthesis: Imaging assessment with clinical X-ray spectra. Phys Medica 2022;98:88–97.
[14] Mettivier G, Sarno A, Varallo A, Russo P. Attenuation coefficient in the energy range 14-36 keV of 3D printing materials for physical breast phantoms. Phys Med Biol 2022;67.
[15] Ma XJ, Buschmann M, Unger E, Homolka P. Classification of X-ray attenuation properties of additive manufacturing and 3D printing materials using computed tomography from 70 to 140 kVp. Front Bioeng Biotech 2021;9.
[16] Ma X, Figl M, Unger E, Buschmann M, Homolka P. X-ray attenuation of bone, soft and adipose tissue in CT from 70 to 140 kV and comparison with 3D printable additive manufacturing materials. Sci Rep 2022;12:14580.
[17] Okkalidis F, Chatzigeorgiou C, Okkalidis N, Dukov N, Milev M, Bliznakov Z, et al. Characterization of commercial and custom-made printing filament materials for computed tomography imaging of radiological phantoms. Technologies 2024;12.
[18] Morphe. https://morphe.cc/.
[19] TPC. https://formfutura.com/c/filaments/tpc-filaments/.
[20] Marinov S, Buliev I, Cockmartin L, Bosmans H, Bliznakov Z, Mettivier G, et al. Radiomics software for breast imaging optimization and simulation studies. Phys Medica 2021;89:114–28.
[21] Chen L, Abbey CK, Nosratieh A, Lindfors KK, Boone JM. Anatomical complexity in breast parenchyma and its implications for optimal breast imaging strategies. Med Phys 2012;39:1435–41.
[22] Chen L, Abbey CK, Boone JM. Association between power law coefficients of the anatomical noise power spectrum and lesion detectability in breast imaging modalities. Phys Med Biol 2013;58:1663–81.
[23] Metheany KG, Abbey CK, Packard N, Boone JM. Characterizing anatomical variability in breast CT images. Med Phys 2008;35:4685–94.
[24] Mettivier G, Bliznakova K, Sechopoulos I, Boone JM, Di Lillo F, Sarno A, et al. Evaluation of the BreastSimulator software platform for breast tomography. Phys Med Biol 2017;62:6446–66.
[25] Bliznakova K, Georgiev T, Sarno A, Teneva T, Dukov N, Okkalidis N, et al. A comparison of two low-cost 3D printing techniques for constructing phantoms from MRI breast images. Intl J Radiat Res 2024;22:883–90.
[26] Dukov N, Bliznakova K, Baneva Y, Bliznakov Z. Influence of the 3D printing infill, pattern and CT kV on the Hounsfield Units for biomedical applications. 20th Nordic-Baltic Conference on Biomedical Engineering and the 24th Polish Conference on Biocybernetics and Biomedical Engineering (NBC 2025 & PCBBE 2025). Warshav, Poland. 2025.
[27] Kunert P, Trinkl S, Giussani A, Reichert D, Brix G. Tissue equivalence of 3D printing materials with respect to attenuation and absorption of X-rays used for diagnostic and interventional imaging. Med Phys 2022;49:7766–78.
[28] Bliznakova K, Suryanarayanan S, Karellas A, Pallikarakis N. Evaluation of an improved algorithm for producing realistic 3D breast software phantoms: application for mammography. Med Phys 2010;37:5604–17.
[29] Boone JM, Lindfors KK, Beatty CS, Seibert JA. A breast density index for digital mammograms based on radiologists' ranking. J Digit Imaging 1998;11:101–15.
[30] Caldwell CB, Stapleton SJ, Holdsworth DW, Jong RA, Weiser WJ, Cooke G, et al. Characterisation of mammographic parenchymal pattern by fractal dimension. Phys Med Biol 1990;35:235–47.